

MIC-BEV: Multi-Infrastructure Camera Bird's-Eye-View Transformer with Relation-Aware Fusion for 3D Object Detection

Yun Zhang, Zhaoliang Zheng, Johnson Liu, Zhiyu Huang*,
Zewei Zhou, Zonglin Meng, Tianhui Cai, and Jiaqi Ma

Abstract—Infrastructure-based perception plays a crucial role in intelligent transportation systems, offering global situational awareness and enabling cooperative autonomy. However, existing camera-based detection models often underperform in such scenarios due to challenges such as multi-view infrastructure setup, diverse camera configurations, degraded visual inputs, and various road layouts. We introduce MIC-BEV, a Transformer-based bird's-eye-view (BEV) perception framework for infrastructure-based multi-camera 3D object detection. MIC-BEV flexibly supports a variable number of cameras with heterogeneous intrinsic and extrinsic parameters and demonstrates strong robustness under sensor degradation. The proposed graph-enhanced fusion module in MIC-BEV integrates multi-view image features into the BEV space by exploiting geometric relationships between cameras and BEV cells alongside latent visual cues. To support training and evaluation, we introduce M2I, a synthetic dataset for infrastructure-based object detection, featuring diverse camera configurations, road layouts, and environmental conditions. Extensive experiments on both M2I and the real-world dataset RoScenes demonstrate that MIC-BEV achieves state-of-the-art performance in 3D object detection. It also remains robust under challenging conditions, including extreme weather and sensor degradation. These results highlight the potential of MIC-BEV for real-world deployment. The dataset and source code are available at: <https://github.com/HandsomeYun/MIC-BEV>.

Index Terms—BEV perception, Infrastructure-based sensing, 3D object detection, Graph-enhanced fusion

I. INTRODUCTION

INFRASTRUCTURE-based perception is a key enabler for intelligent transportation systems, providing critical support for traffic monitoring, situational awareness, and cooperative autonomy in urban environments [1]–[3]. Sensors deployed at intersections, crosswalks, and merging zones offer a strategic advantage for observing traffic participants from elevated viewpoints, providing broader and more stable observations. This spatial advantage facilitates long-term monitoring and enhances the ability to detect dynamic objects [4]. Although LiDAR sensors have been widely adopted for infrastructure-based object detection due to their accurate 3D measurements, they remain costly, maintenance-intensive, and sensitive to mounting and calibration errors [5]–[7]. In contrast, cameras are significantly more affordable, scalable, and easier to deploy. They also provide rich semantic information that enhances scene understanding in large-scale sensing applications,

All authors are with the University of California, Los Angeles (UCLA), CA 90095, USA. Email: {yun66, zhz03, jwu7, zhiyu, zewei, meng925, tianhui, jiaqima}@ucla.edu

*Corresponding author: Zhiyu Huang.

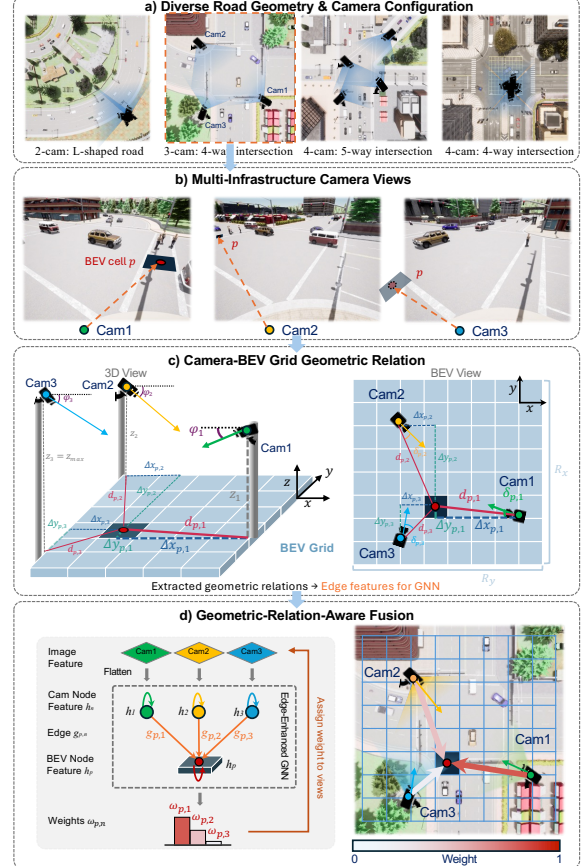


Fig. 1: Overview of the proposed MIC-BEV framework for multi-camera infrastructure perception. (a) Example scenarios of infrastructure sensing with diverse road geometry and camera configuration. (b) Multiple cameras capture the scene from different viewpoints and project objects onto a defined BEV grid. (c) MIC-BEV encodes the geometric relations between each camera and BEV cell, such as distances, angles, and height differences, to construct edge features for a graph neural network (GNN). (d) The GNN in MIC-BEV performs geometric relation-aware fusion, assigning importance weights to each camera for adaptive multi-view feature aggregation.

making them an attractive alternative for infrastructure-based perception [8].

While single-camera infrastructure perception systems have been extensively studied [9]–[11], their spatial coverage and robustness are inherently limited, particularly under occlusion

or in complex scenes. Multi-camera infrastructure sensing addresses these limitations by integrating information from multiple viewpoints to achieve more comprehensive and resilient scene understanding [12]. Nonetheless, it introduces several critical challenges. **1) Spatially distributed sensors.** Cameras deployed across large spatial distances often have overlapping fields of view with significant perspective differences and occlusions. These multi-view conditions make spatial alignment and feature fusion across views challenging. **2) Variability in camera configurations.** Unlike vehicle-mounted sensors that follow consistent mounting patterns, infrastructure cameras are deployed with diverse quantities, spatial layouts, orientations, fields of view (FoV), and degrees of overlap. Each intersection has a distinct design, requiring models to adapt to a wide range of installation configurations. **3) Sensor reliability and robustness.** Infrastructure cameras may degrade or fail over time without immediate detection or repair. Therefore, perception models must maintain robustness against missing, corrupted, or low-quality visual inputs during real-world deployment.

To address these challenges, we propose **MIC-BEV** (Multi-Infrastructure Camera Bird’s-Eye-View Transformer), an effective 3D object detection model for infrastructure-based multi-camera perception using a Bird’s-Eye-View (BEV) representation. MIC-BEV introduces a **relation-enhanced spatial cross-attention** mechanism that fuses multi-view features by jointly considering camera-specific embeddings and their geometric relations with each BEV cell through a graph neural network (GNN) [13], as illustrated in Fig. 1. This enables adaptive weighting of information from heterogeneous camera viewpoints and improves multi-view feature aggregation. MIC-BEV further incorporates both map-level and object-level BEV segmentation to enhance spatial understanding. In addition, MIC-BEV adapts to diverse camera and road layouts and employs camera masking strategies such as random dropout and Gaussian blur during training to improve robustness against occlusion, sensor degradation, and camera failure.

To overcome the scarcity of real-world datasets that capture diverse infrastructure configurations, weather conditions, and camera layouts, we introduce **M2I**, a large-scale synthetic dataset for Multi-camera, Multi-layout Infrastructure perception. M2I covers a wide range of infrastructures with variations in camera quantity, spatial layout, heading angle, FoV, and degrees of overlap, as well as challenging conditions such as adverse weather and varying lighting. This dataset provides a comprehensive benchmark for model training and evaluation. The main contributions of this paper are summarized as:

- 1) We propose **MIC-BEV**, a BEV-based 3D object detection model for multi-camera infrastructure perception that fuses heterogeneous multi-view observations using spatial cross-attention enhanced with graph-based relation modeling and fusion.
- 2) We introduce **M2I**, a large-scale synthetic dataset featuring diverse and realistic multi-camera settings and scene conditions, enabling comprehensive evaluation of model generalization and robustness.
- 3) We conduct comprehensive experiments on the M2I dataset and real-world RoScenes dataset, demonstrating

that MIC-BEV achieves strong and consistent performance, and validating its adaptability to heterogeneous infrastructure layouts and robustness.

II. RELATED WORK

A. Camera-based BEV Perception

BEV representations have become a dominant paradigm in camera-based 3D perception, offering a unified spatial abstraction across multi-view inputs. Early works such as OFT [14] and CADDN [15] project monocular image features into BEV space to enable 3D object detection. Lift-Splat-Shoot [16] advances this by lifting 2D image features into 3D frustums using predicted depth distributions and projecting them into BEV space through vertical accumulation, while BEVDet [17] improves efficiency for multi-view settings. BEVDepth [18] further enhances depth modeling through LiDAR-guided supervision, and GeBEV [19] improves the geometric fidelity of BEV representations via radial-Cartesian sampling and centroid-aware depth supervision.

Transformer-based methods further advance BEV detection. DETR3D [20] extends DETR [21] to 3D detection by sampling image features at learned 3D reference points through deformable attention, removing the need for explicit depth estimation. PETR [22] introduces 3D positional encodings to lift 2D features into a pseudo-3D space, while PETRv2 [23] adds depth supervision and improved alignment for multi-view fusion. BEVFormer [24], proposed shortly after PETR, establishes a strong foundation for BEV-based perception by introducing learnable BEV queries and spatiotemporal deformable attention for dense and temporally consistent feature fusion. Subsequent methods explore complementary directions for improving temporal reasoning and efficiency. StreamPETR [25] extends PETR with a memory-based temporal stream for video inference. In contrast, BEVDet4D [26], SoloFusion [27], and BEVNext [28] follow the dense BEV-based paradigm, enhancing depth modeling, long-term temporal fusion, and multi-view feature efficiency, respectively.

While these methods achieve impressive results in ego-centric, vehicle-mounted scenarios, they typically assume fixed and calibrated camera layouts surrounding the ego vehicle. In contrast, infrastructure-based systems deploy spatially distributed cameras with diverse orientations, heights, and fields of view, which vary significantly across intersections, road geometries, and installation sites. Such heterogeneity introduces substantial challenges for geometric alignment and multi-view feature fusion, motivating the development of BEV perception frameworks specifically designed for infrastructure-based environments.

B. Infrastructure-based 3D Perception and Datasets

Infrastructure-based perception systems often rely on LiDAR [29]–[31] or LiDAR-camera fusion for 3D object detection [32]–[35]. However, due to the high deployment cost of LiDAR and its lack of semantic information, camera-only approaches are gaining growing interest [11], [36], [37]. Early efforts focused on monocular 3D detection using datasets such as Rope3D [38] and DAIR-V2X [39]. Methods like BEVHeight

[40], BEVHeight++ [41], and CoBEV [42] enhance spatial understanding by leveraging depth-height cues. More recently, MonoUNI [43] introduces normalized depth features to reduce reliance on explicit height cues, achieving better generalization from infrastructure to vehicle perspectives.

Recent simulation-based datasets such as AgentVerse [44] and cooperative datasets such as V2XVerse [45] extend this direction by modeling heterogeneous infrastructures and vehicle–infrastructure coordination under diverse weather and traffic conditions. At the same time, multi-camera configurations have emerged as a practical solution for expanding spatial coverage and improving robustness. Existing datasets such as V2X-Real [46] and RCOPPER [47] explore multi-camera perception in single-intersection and corridor environments, while RoScenes [48] targets highway scenes. Calibration-free frameworks [49] further alleviate dependence on precise extrinsic calibration, and occupancy-based approaches such as MC-BEVRO [50] highlight the potential of infrastructure-mounted cameras for large-scale traffic monitoring. More recently, RoBEV and RopeBEV [51] establish strong baselines by fusing multi-view features using feature-guided queries and rotation-aware embeddings, respectively.

However, existing multi-camera fusion strategies are largely implicit and lack interpretability at the per-view level. In addition, the spatial and environmental diversity of current infrastructure-based datasets is narrow, typically restricted to a single scene with fixed infrastructure arrangements and limited weather or lighting variation. These constraints hinder model generalization across heterogeneous infrastructures and real-world deployment conditions. To address these challenges, we introduce the **M2I** dataset, which encompasses a wide range of intersection types, camera configurations, and environmental conditions. We propose **MIC-BEV**, a relation-aware-fusion BEV framework that leverages a GNN to capture geometric dependencies among cameras and dynamically infer per-view fusion weights, enabling interpretable and adaptive multi-view fusion across diverse infrastructure scenarios.

III. METHODOLOGY

A. Problem Definition

The objective of this work is to develop a multi-camera 3D object detection model for infrastructure-mounted sensors, augmented with a BEV segmentation task to enhance spatial reasoning. Given a set of synchronized multi-view RGB images, the model $\text{Det}(\cdot)$ jointly predicts a set of 3D bounding boxes \hat{B} and a BEV segmentation \hat{M} :

$$\hat{B}, \hat{M} = \text{Det}_\phi \left(\{(I_n, E_n, K_n)\}_{n=1}^N \right), \quad (1)$$

where I_n is the RGB image from the n -th camera, E_n and K_n are the corresponding extrinsic and intrinsic matrices, and ϕ denotes the learnable parameters of the model. The number of cameras N varies across different scenes.

The primary task is 3D object detection, which involves predicting a set of bounding boxes \hat{B} in a shared BEV coordinate frame. Each box \hat{B}_i is parameterized as $\hat{B}_i = (x, y, z, l, w, h, \psi)$, where (x, y, z) denotes the object's position, (l, w, h) its bounding box dimensions, and ψ its yaw

angle. To support spatial understanding, we formulate a BEV semantic segmentation task with two complementary levels: map-level and object-level. The model predicts a semantic map $\hat{M} = [\hat{M}_{\text{map}}, \hat{M}_{\text{object}}]$, where $\hat{M}_{\text{map}} \in \mathbb{R}^{N_{\text{map}} \times H_{\text{bev}} \times W_{\text{bev}}}$ captures static map semantics (e.g., road, crosswalk), and $\hat{M}_{\text{object}} \in \mathbb{R}^{N_{\text{object}} \times H_{\text{bev}} \times W_{\text{bev}}}$ captures dynamic objects (e.g., vehicle, pedestrian). Each BEV cell predicts a class-wise probability distribution for both static and dynamic elements, allowing the model to reason jointly about the environment and the spatial distribution of objects.

B. Overall Architecture

MIC-BEV is designed for infrastructure-mounted cameras with diverse road layouts and spatial configurations, where viewpoints are highly heterogeneous and fields of view vary across scenes. As shown in Fig. 2, the model comprises three main components: 1) an image backbone for multi-view feature extraction, 2) a Transformer encoder that aggregates image features into a unified BEV representation through temporal modeling and relation-enhanced spatial attention, and 3) task-specific decoding heads for 3D object detection and BEV segmentation.

Unlike BEVFormer [24], which is designed for vehicle-mounted cameras with fixed and calibrated views, MIC-BEV is specifically tailored for infrastructure-based perception, where camera poses, heights, and orientations differ across scenes. To address this variability, MIC-BEV incorporates a **relation-enhanced attention** mechanism that models geometry-aware relations between each camera and BEV cell, such as the relative distance and viewing angle, through a GNN. This design enables the model to adaptively weight features from multiple cameras according to their geometric relevance to each BEV cell.

C. Variable Multi-Camera Inputs

Infrastructure sensing systems often operate with varying numbers of cameras and heterogeneous fields of view, depending on intersection layouts or deployment constraints. To ensure adaptability, MIC-BEV is designed to handle a dynamic set of input cameras. When the number of available cameras is fewer than the maximum supported (N_{max}), we pad the input with dummy images (zero-valued tensors) and assign identity matrices as their calibration parameters. These placeholders are effectively ignored in downstream spatial attention and graph computations by ensuring that their 3D projections produce non-positive depths, thereby excluding them from the set of valid contributing views \mathcal{V}_{hit} (see Section III-D).

To improve robustness, we introduce a view-masking augmentation during training to simulate sensor degradation or temporary camera failures. For each training sample, with probability p_m , one camera view is randomly selected and either replaced with a zero-valued image or blurred using a Gaussian kernel; with probability $1 - p_m$, all views remain unchanged. This strategy encourages MIC-BEV to adaptively rely on the available camera views, improving resilience to missing or degraded inputs while maintaining full performance when all cameras are operational.

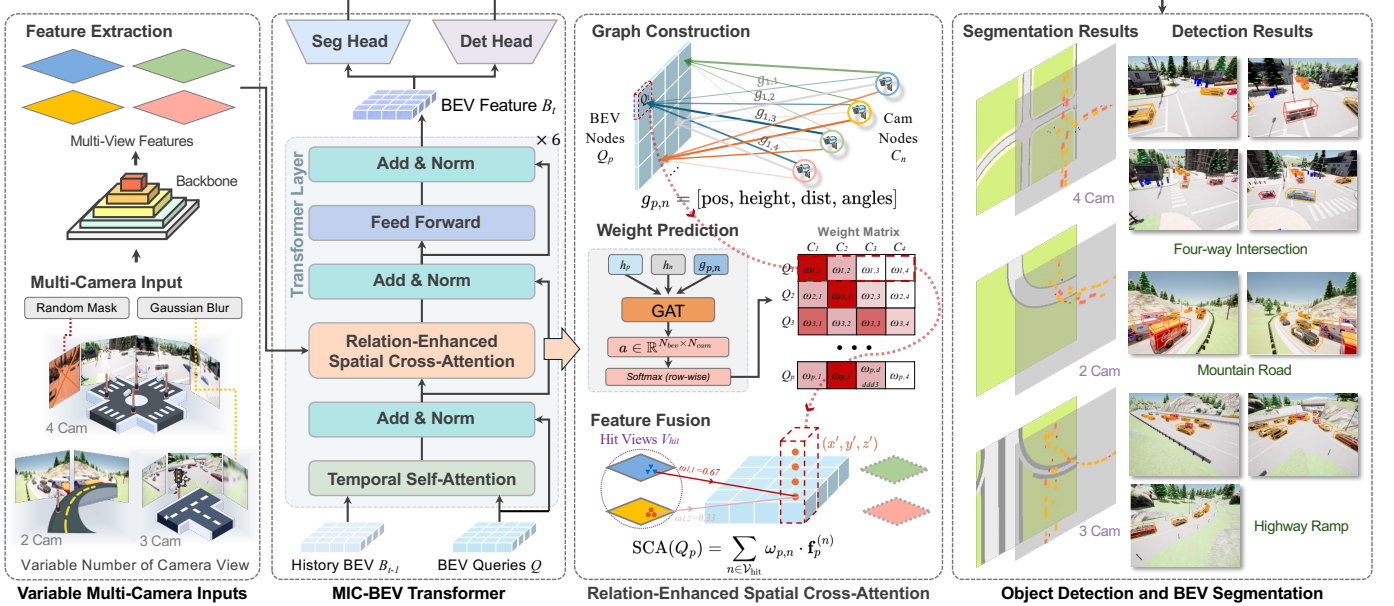


Fig. 2: **Overview of the MIC-BEV architecture.** The model takes multi-view images from a variable number of infrastructure-mounted cameras as input and extracts features through a shared backbone. A camera masking module applies random dropout or Gaussian noise to simulate degraded views. The extracted features are fused into a BEV representation via Transformer layers with temporal self-attention and our proposed **Relation-Enhanced Spatial Cross-Attention**. GAT networks are used to dynamically assign view-dependent weights based on camera node features and geometric relations between the camera and its visible BEV cells. The resulting BEV features are used for both object detection and BEV semantic segmentation tasks.

D. MIC-BEV Transformer

The process of encoding multi-camera features into BEV space in MIC-BEV is summarized in Algorithm 1. The Transformer model is designed to handle heterogeneous camera configurations while preserving spatial and temporal consistency.

1) **Encoder and BEV Queries:** We employ a ResNet-101 [52] backbone coupled with a Feature Pyramid Network (FPN) [53] to extract multi-scale features from each camera image. The BEV representation is defined as a 2D grid anchored to the ground plane and centered at the scene. We initialize a learnable tensor $\mathbf{Q} \in \mathbb{R}^{H_{\text{bev}} \times W_{\text{bev}} \times C}$ to represent the grid, where H_{bev} and W_{bev} denote the grid resolution, and C is the feature dimension. Each cell $Q_p \in \mathbb{R}^C$ serves as a latent query corresponding to a grid location $p = (x, y)$ in the BEV space. These BEV queries interact with multi-view image features via spatial cross-attention and are iteratively refined to capture spatial cues encoded by the mounted cameras.

2) **Temporal Self-Attention:** To capture object moving dynamics, temporal self-attention (TSA) allows current BEV queries Q to attend to the previous BEV map B_{t-1} . In static infrastructure setups, this is simplified without ego-motion compensation. Incorporating temporal context helps recover occluded or intermittently visible objects and stabilizes predictions over consecutive frames.

3) **Relation-Enhanced Spatial Cross-Attention:** Given a set of multi-view camera feature maps $\{F^{(n)}\}_{n=1}^N$, the proposed Relation-Enhanced Spatial Cross-Attention (ReSCA) aggregates them into a unified BEV representation $F \in \mathbb{R}^{C \times H_{\text{bev}} \times W_{\text{bev}}}$. For each BEV query Q_p located at p in the BEV grid, we generate a vertical stack of N_{ref} 3D reference

points $\mathbf{r}_{p,j} = (x, y, z_j)$ using a predefined set of anchor heights $\{z_j\}_{j=1}^{N_{\text{ref}}}$. These pillars help capture semantic features across different heights. Each 3D reference point $\mathbf{r}_{p,j}$ is projected onto the n -th camera view as 2D coordinates $\mathbf{u}_{p,j}^{(n)}$. Only camera views where the projected points fall within valid image bounds are included in the hit-view set $\mathcal{V}_{\text{hit}} \subseteq 1, \dots, N$.

For each hit view $n \in \mathcal{V}_{\text{hit}}$, we apply deformable attention (DeformAttn) [54] around the projected locations $\{\mathbf{u}_{p,j}^{(n)}\}_{j=1}^{N_{\text{ref}}}$ of 3D reference points associated with BEV query Q_p . This produces a per-view feature $\mathbf{f}_p^{(n)} \in \mathbb{R}^C$.

Graph Construction. To adaptively weigh the contribution of each camera view for every BEV cell, we formulate the fusion process as a bipartite graph attention problem. The conventional uniform averaging of multi-view features ignores how *informative* or *reliable* each view is, especially under occlusions or perspective bias. We therefore learn the fusion weights $\omega_{p,n}$ using a geometry- and content-aware Graph Attention Network (GAT) [55].

We construct a bipartite graph $\mathcal{G} = (\mathcal{V}_{\text{cam}}, \mathcal{V}_{\text{bev}}, \mathcal{E})$, where each camera node $C_n \in \mathcal{V}_{\text{cam}}$ represents a pooled image feature map from camera n , and each BEV grid cell node $Q_p \in \mathcal{V}_{\text{bev}}$ is represented by a BEV query located at p . The node features are defined as:

$$\mathbf{h}_p = Q_p \in \mathbb{R}^C \quad \text{for BEV nodes,} \quad (2)$$

$$\mathbf{h}_n = \frac{1}{K} \sum_{k=1}^K f_{n,k} \in \mathbb{R}^C \quad \text{for camera nodes,} \quad (3)$$

where $K = H \times W$ is the number of tokens from the camera feature map $F^n \in \mathbb{R}^{C \times H \times W}$, with H and W denoting the

Algorithm 1: Forward Pass of MIC-BEV Encoding

Input: $\{\mathbf{B}_{t-k}\}_{k=1}^T$: past T frames BEV history queue;
 $\{\mathbf{F}^{(n)}\}_{n=1}^{N_{\text{cam}}}$: multi-view image features;
 $\{\mathbf{K}_n, \mathbf{E}_n\}_{n=1}^N$: intrinsics/extrinsics;
 L : number of Transformer layers;
 N_{ref} : number of anchor heights

Output: \mathbf{B}_{out} : current-frame BEV features

- 1. Generate reference points**
 $\mathbf{r}^{3D} \leftarrow \text{GETREFPOINTS3D}(H_{\text{bev}}, W_{\text{bev}}, N_{\text{ref}})$;
// Shape: $[N_{\text{ref}}, H_{\text{bev}}, W_{\text{bev}}, 3]$
- 2. Project 3D anchors to camera views (once)**
 $\{\{\mathbf{u}_n, \mathbf{m}_n\}\}_{n=1}^N \leftarrow \text{POINTSAMPLING}(\mathbf{r}^{3D}, \{\mathbf{K}_n, \mathbf{E}_n\})$
; // \mathbf{m}_n masks invalid points
- 3. Initialize temporal references (static cameras)**
if $T > 0$ **then**
| $\mathbf{B}_{\text{prev}} \leftarrow \text{CONCAT}(\{\mathbf{B}_{t-k}\}_{k=1}^T)$
else
| $\mathbf{B}_{\text{prev}} \leftarrow \text{ZEROSLIKE}(\mathbf{Q})$
- 4. Transformer layers**
 $\mathbf{B}_0 \leftarrow \mathbf{Q}$; // Initialize with learnable BEV queries
for $\ell = 1$ **to** L **do**
| // Temporal Self-Attention (TSA)
| $\mathbf{B}_\ell \leftarrow \text{TSA}(\mathbf{B}_{\ell-1}, \mathbf{B}_{\text{prev}})$;
| $\mathbf{B}_\ell \leftarrow \text{NORM}(\mathbf{B}_\ell)$;
| // Relation-Enhanced Spatial Cross-Attention (ReSCA)
| $\mathbf{B}_\ell \leftarrow \text{RESCA}(\mathbf{B}_\ell, \{\mathbf{F}^{(n)}\}, \mathbf{r}^{3D}, \{\mathbf{u}_n\}, \{\mathbf{m}_n\})$
| $\mathbf{B}_\ell \leftarrow \text{NORM}(\mathbf{B}_\ell)$;
| // Feed-Forward Network (FFN)
| $\mathbf{B}_\ell \leftarrow \text{FFN}(\mathbf{B}_\ell)$;
| $\mathbf{B}_\ell \leftarrow \text{NORM}(\mathbf{B}_\ell)$;

return \mathbf{B}_L

height and width of the feature map, respectively. $f_{n,k}$ denotes the k -th token feature from camera n .

Edges \mathcal{E} are directed from cameras to visible BEV nodes, $\mathcal{E} = \{(n, p) \mid Q_p \text{ is visible from camera } C_n\}$. Each edge $(n \rightarrow p)$ is annotated with a geometric relation descriptor $\mathbf{g}_{p,n} \in \mathbb{R}^8$, consisting of:

$$\mathbf{g}_{p,n} = \left[\frac{\Delta x_{p,n}}{R_x}, \frac{\Delta y_{p,n}}{R_y}, \frac{z_n}{z_{\max}}, \frac{\|\mathbf{d}_{p,n}\|_2}{\sqrt{R_x^2 + R_y^2}}, \cos \delta_{p,n}, \sin \delta_{p,n}, \cos \varphi_n, \sin \varphi_n \right], \quad (4)$$

where $\mathbf{d}_{p,n} = (\Delta x_{p,n}, \Delta y_{p,n}) = (x_p - x_n, y_p - y_n)$ is the 2D planar offset between the BEV grid and the camera center. R_x and R_y are normalization constants corresponding to the sensing range in x and y directions, used to scale spatial offsets to a consistent range within $[-1, 1]$. Similarly, z_n is the camera's height, normalized by the maximum camera height z_{\max} . $\delta_{p,n}$ is the heading difference between the camera's yaw and the angle from camera n to the BEV cell at location p , and φ_n is the pitch angle of camera n . To ensure rotational continuity and avoid discontinuities near $\pm\pi$, we use heading with its sine and cosine components, i.e., $\cos \delta_{p,n}$ and $\sin \delta_{p,n}$.

By jointly normalizing geometric features, we ensure that the network is invariant to map scale, BEV resolution, and elevation difference, enabling generalization across scenes with different layouts or camera setups.

Algorithm 2: Camera-to-BEV Fusion Weights via GAT

Input: $\mathbf{Q} \in \mathbb{R}^{B \times N_q \times C}$: BEV queries;
 $\{\mathbf{F}^{(n)}\}_{n=1}^{N_{\text{cam}}} \in \mathbb{R}^{B \times C \times H \times W}$: camera features;
 $\mathbf{M} \in \{0, 1\}^{B \times N_q \times N_{\text{cam}}}$: BEV visibility mask;
 $(\mathbf{P}, \psi, \varphi)$: camera positions, yaw, pitch; f_θ : GATv2
Output: $\mathbf{W} \in \mathbb{R}^{B \times N_q \times N_{\text{cam}}}$: fusion weights

- 1. Node features:** Mean-pool image tokens to get camera embeddings $\mathbf{C}_b[n] = \frac{1}{HW} \sum_{h,w} \mathbf{F}_{b,:,h,w}^{(n)}$; use \mathbf{Q}_b as BEV node features.
- 2. Edges:** From the visibility mask
 $\mathcal{E}_b = \{(n \rightarrow q) \mid \mathbf{M}_{b,q,n} = 1\}$ (connect visible cameras to BEV cells).
- 3. Edge attributes:** For each edge (b, q, n) compute geometry vector
 $\mathbf{g}_{b,q,n} = [\frac{\Delta x}{R_x}, \frac{\Delta y}{R_y}, \frac{z_n}{z_{\max}}, \frac{\|\mathbf{d}\|_2}{\sqrt{R_x^2 + R_y^2}}, \cos \delta, \sin \delta, \cos \varphi, \sin \varphi]$.
- 4. GAT propagation:**
 $\mathbf{S}_b = f_\theta(\mathbf{Q}_b, \mathbf{C}_b, \mathcal{E}_b, \mathbf{g}_b) \in \mathbb{R}^{N_q \times N_{\text{cam}}}$.
- 5. Normalization:** Mask invalid edges ($\mathbf{S}_{b,q,n} = -\infty$ if $\mathbf{M}_{b,q,n} = 0$), Then apply softmax across cameras:
 $\mathbf{W}_{b,q,:} = \text{softmax}_n(\mathbf{S}_{b,q,:})$.

return \mathbf{W} .

Weight Prediction. We employ a GAT network f_θ to model the interaction between each BEV node, camera node, and their geometric relation, as detailed in Algorithm 2. Specifically, f_θ is instantiated as a GATv2 [56] with three layers, four attention heads per layer, and 128 hidden units.

Node features \mathbf{h}_p (BEV) and \mathbf{h}_n (camera) are first projected to 128-dimensional embeddings using a shared 1×1 convolution. Each GATv2 layer incorporates ELU activation, dropout, and residual connections to ensure stable training and effective message passing across the graph.

The network outputs a scalar logit $s_{p,n}$ for each relation pair $(n \rightarrow p)$, representing the importance weight of the camera node n for the BEV cell p :

$$s_{p,n} = f_\theta(\mathbf{h}_p, \mathbf{h}_n, \mathbf{g}_{p,n}). \quad (5)$$

The logits are reshaped to (B, N_q, N_{cam}) and normalized across cameras using a visibility-aware softmax. For non-visible cameras, we set $s_{p,n} \leftarrow -\infty$ to exclude them. The final fusion weights $\omega_{p,n}$ are then computed as:

$$\omega_{p,n} = \frac{\exp(s_{p,n})}{\sum_{n' \in \mathcal{V}_{\text{hit}}} \exp(s_{p,n'})}. \quad (6)$$

This formulation enables adaptive weighting across multiple camera views, where each BEV cell dynamically attends to the most informative and geometrically relevant viewpoints.

Feature Fusion. The final BEV feature is computed by fusing all visible views with learned weights $\omega_{p,n}$:

$$\text{ReSCA}(Q_p) = \sum_{n \in \mathcal{V}_{\text{hit}}} \omega_{p,n} \cdot \mathbf{f}_p^{(n)}, \sum_n \omega_{p,n} = 1, \quad (7)$$

$$\mathbf{f}_p^{(n)} = \sum_{j=1}^{N_{\text{ref}}} \text{DeformAttn}(Q_p, \mathbf{u}_{p,j}^{(n)}, F_t^{(n)}).$$

This geometry- and content-aware fusion strategy enables the model to selectively emphasize the most informative and geometrically favorable camera views, while suppressing occluded or degraded inputs. As a result, the fused BEV representation becomes more robust, interpretable, and reliable across a wide range of camera configurations.

E. Object Detection and BEV Segmentation

The BEV Transformer layers output a shared BEV feature map $B_t \in \mathbb{R}^{C \times H_{\text{bev}} \times W_{\text{bev}}}$, which serves as a unified representation for both object detection and BEV segmentation. Two task-specific convolutional decoders operate in parallel on this shared feature map. Each decoder comprises four stacked 3×3 convolutional blocks with Group Normalization and ReLU activations, followed by a 1×1 classification layer. The decoders operate at full BEV resolution without upsampling.

1) **Detection Head:** For object detection, we adopt a DETR-style decoder [21] with N_q object queries. Each query outputs a class probability vector $\hat{y} \in \mathbb{R}^{n_{\text{obj}}+1}$ including a background class, and bounding box attributes \hat{b} .

The detection loss \mathcal{L}_{det} follows a DETR-style bipartite matching formulation:

$$\mathcal{L}_{\text{det}} = \lambda_{\text{cls}} \mathcal{L}_{\text{cls}} + \lambda_{\text{reg}} \mathcal{L}_{\text{reg}}, \quad (8)$$

where \mathcal{L}_{cls} is a focal loss with weight $\lambda_{\text{cls}} = 2.0$ and \mathcal{L}_{reg} is an L1 loss with weight $\lambda_{\text{reg}} = 0.25$.

2) **Segmentation Head:** For segmentation, the model predicts static map logits $\hat{M}_{\text{map}} \in \mathbb{R}^{n_{\text{map}} \times H \times W}$ and dynamic object logits $\hat{M}_{\text{object}} \in \mathbb{R}^{(n_{\text{obj}}+1) \times H \times W}$. The corresponding ground-truth masks $M_{\text{map}}, M_{\text{object}}$ are derived from rasterized HD maps and instance annotations. In practice, we apply bilinear interpolation to align the decoder outputs with the label map dimensions when necessary. The segmentation loss is defined as:

$$\mathcal{L}_{\text{seg}} = \text{CE}(\hat{M}_{\text{map}}, M_{\text{map}}) + \text{CE}(\hat{M}_{\text{object}}, M_{\text{object}}), \quad (9)$$

where $\text{CE}(\cdot, \cdot)$ denotes standard softmax cross-entropy.

The model is trained with a combined multi-task loss:

$$\mathcal{L} = \mathcal{L}_{\text{det}} + \lambda \mathcal{L}_{\text{seg}}, \quad (10)$$

where $\lambda = 2$ is the task balance weight.

IV. DATASETS

A. Limitations of Existing Infrastructure Sensing Datasets

Existing datasets only partially reflect the complexity of real-world infrastructure perception, hindering the generalization of learned models across diverse deployment scenarios. The main limitations can be grouped into three categories:

restricted camera configurations, limited scene diversity, and insufficient environmental variation.

Limited camera configuration. Existing infrastructure datasets exhibit limited variability in camera setups, often relying on single static viewpoints or fixed multi-camera arrangements. Monocular camera datasets such as Rope3D [38] and DAIR-V2X-I [39] use a single stationary camera, leading to narrow spatial coverage and no possibility for cross-view fusion. Multi-camera datasets, including RCooper [47], V2X-Real [60], and V2X-PnP [58], place cameras at a single intersection with fixed geometry, providing no variation in setup across different environments. In both cases, camera layouts, heights, and orientations remain homogeneous, limiting model adaptability to diverse road geometries and deployment conditions in the real world.

Limited scene diversity. Beyond camera setup, existing datasets capture only a narrow range of spatial and contextual environments. Intersection-focused datasets such as RCooper [47], V2X-Real [60], and V2X-PnP [58] are recorded at a single, fixed intersection, where the same geometry, layout, and surroundings appear throughout the dataset. Similarly, highway-focused datasets like RoScenes [48] are limited to one highway with linear road topology and low interaction density, lacking complex cross-traffic or vulnerable road users such as pedestrians and cyclists. As a result, these benchmarks offer minimal variation in spatial layout or contextual diversity, constraining the development of perception models capable of generalizing across diverse real-world road environments.

Limited dynamic conditions. Most existing infrastructure datasets are collected primarily under clear daytime conditions, providing limited variation in illumination or weather. Adverse environments such as heavy rain and dense fog are typically excluded, while dusk and night scenes appear only sparsely. Consequently, models trained on these datasets often struggle to handle realistic illumination changes, sensor noise, and dynamic temporal variations that critically affect perception robustness in practice.

B. M2I Dataset

To address these limitations, we introduce the **M2I (Multi-camera Multi-layout Infrastructure) Perception Dataset**, a large-scale benchmark explicitly designed for 3D perception across heterogeneous roadside environments. Table I summarizes a comparison of M2I with prior infrastructure-based and V2X perception datasets.

M2I contains 278K frames, 927K images, and 11.5 million annotated bounding boxes, each paired with synchronized RGB cameras, LiDAR, 3D bounding boxes, and semantic BEV maps. It includes 1,103 scenario clips covering a wide spectrum of road geometries. Each clip spans 200-300 frames (10 Hz) with an average of 40 road users, covering multiple object classes such as cars, trucks, pedestrians, and cyclists. M2I supports tasks including 3D object detection, semantic segmentation, multi-object tracking, and trajectory prediction. The dataset is divided into 772 training, 110 validation, and 221 test scenarios using a 7:1:2 ratio at the clip level to ensure temporal consistency and reproducibility.

TABLE I: Comparison of infrastructure perception datasets. Weather and map availability are key attributes, while variation captures diversity across layouts, locations, and fields of view. Prior datasets often have fixed camera setups and narrow scene types, whereas **M2I** offers broader diversity and richer supervision.

Dataset	Type	Year	Frames	Boxes	# Cams	Extreme Weather	Map	Vary Layouts	Vary Locations	Vary FoVs
V2X-Sim-I [3]	Sim	2022	60K	26.6K	4					✓
V2XSet-I [57]	Sim	2022	44K	233K	4					✓
DAIR-V2X-I [39]	Real	2022	10K	493K	1					✓
Rope3D [38]	Real	2022	50K	1.5M	1					✓
V2X-Real-I [46]	Real	2023	171K	1.2M	4					
V2X-Seq-I [46]	Real	2023	39K	464K	2			✓		
V2X-PnP-I [58]	Real	2024	208K	1.45M	4			✓		
TUMTraf [59]	Real	2024	800	30k	4			✓		
RCooper [47]	Real	2024	50K	242K	2-4				✓	
RoScenes [48]	Real	2024	215K	21.1M	8				✓	✓
M2I (Ours)	Sim	2025	278K	11.6M	1-4	✓	✓	✓	✓	✓



Fig. 3: **Scene diversity in the M2I dataset.** (a) Examples of camera placement configurations across various intersection types, ranging from single-camera highway ramps to multi-camera urban intersections. (b) Diverse weather and illumination conditions, including rain, fog, dusk, and night scenes, highlighting domain variability. (c) Different levels of image blur representing sensor degradation from light to heavy. These variations illustrate the broad coverage and realism of M2I for infrastructure perception.

Scene Diversity. Collecting large-scale datasets across varied sites is both financially and logically challenging, limiting the availability of geometrically diverse real-world data. Constructed using the CARLA simulator [61], M2I spans 41 locations across 7 towns, each characterized by distinct urban structures and layout styles. These towns differ in spatial scale, architectural form, and traffic context, ranging from compact residential districts to mountainous highways and dense downtown grids.

Across these towns, M2I includes eight categories of road geometries, such as three-way, four-way, and five-way inter-

sections, T-junctions, roundabouts, highway ramps, single-lane rural roads, winding mountain paths, and bridges. Even within the same geometric category, locations differ in intersection size, lane configuration, and contextual elements such as pedestrian crossings and traffic signals. Examples can be seen in Fig. 3 (a). Each location is paired with a semantic BEV map, allowing models to leverage structural and contextual priors for perception. This multi-level diversity captures both large-scale layout variability and fine-grained structural distinctions representative of real-world infrastructure environments.

Camera Configuration Diversity. M2I captures realistic

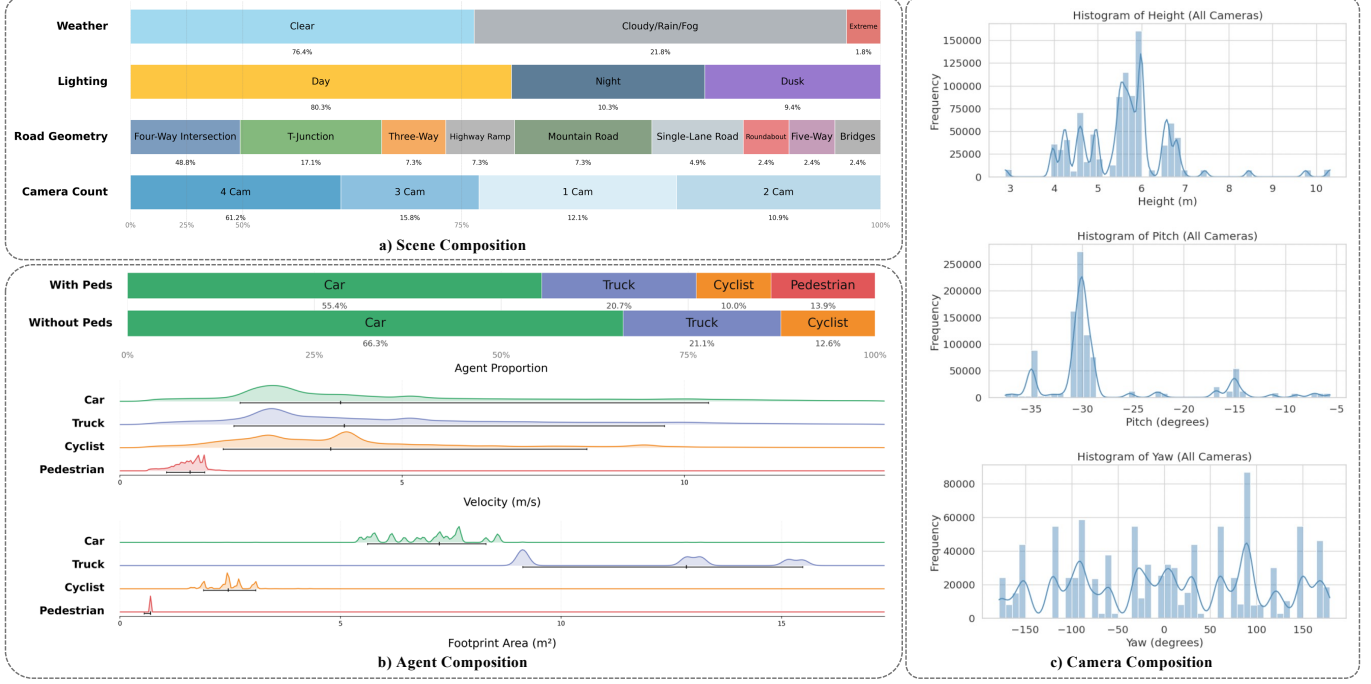


Fig. 4: **M2I Dataset Composition.** (a) Scene composition showing splits by weather, lighting, road geometry, and camera count. (b) Agent composition illustrating class proportions, velocity profiles, and footprint areas across object types. (c) Camera composition showing histograms of camera height, pitch, and yaw across all scenes. These statistics demonstrate the diversity and balance of the M2I dataset for multi-camera perception.

variation in infrastructure-mounted camera setups modeled after common traffic surveillance systems. Each scene contains 1-4 cameras selected from 12 real-world configurations that include typical mounting positions on light poles, traffic lights, and building facades, covering a broad range of heights, orientations, and fields of view.

As illustrated in Fig. 4 (c), camera heights range from 3 m to over 10 m, while pitch angles range from -5° to -35° . The yaw distribution spans nearly the full 360° , indicating coverage of multiple viewing directions rather than fixed orientations.

M2I further introduces intra-geometry variation to emulate realistic deployment differences observed in practice. For instance, in four-way intersections, cameras can be distributed across all four corners [59], aligned along two opposite corners [60], or concentrated near the center [47]. This variation leads to heterogeneous occlusion patterns, asymmetric viewpoints, and diverse visibility ranges, effectively capturing the variability of real-world infrastructure sensors.

Environmental Diversity. Beyond geometric and structural variation, M2I encompasses a wide spectrum of environmental and illumination conditions. The dataset includes diverse weather scenarios such as heavy rain, dense fog, and light drizzle, as well as varying times of day, including dawn, dusk, and night. Examples of these conditions are illustrated in Fig. 3 (b). Such variations introduce visual challenges such as reduced visibility, specular glare, and contrast degradation, which significantly affect object appearance.

To further enhance realism, M2I simulates sensor degradation, including blur caused by adverse weather or aging sensors, as well as temporary sensor dropout and occlusion,

shown in Fig. 3 (c). Traffic density also varies across and within environments: urban scenes feature heavier vehicle and pedestrian flow, while rural and highway settings are comparatively sparse. Each environment includes three traffic levels (low, medium, high) to represent different interaction complexities and occlusion conditions.

This combination of environmental variation, sensor degradation, and traffic diversity establishes M2I as a comprehensive benchmark for evaluating perception models under diverse and dynamically changing real-world conditions.

Object Composition Diversity. As shown in Fig. 4 (b), M2I covers four major object categories: cars, trucks, cyclists, and pedestrians, distributed across a wide range of environments from highways to urban intersections. Each vehicle type includes multiple subcategories, such as sedans, vans, and trailers, reflecting the heterogeneity of traffic participants.

The object proportions in M2I mirror those in large-scale datasets such as nuScenes [62] and Waymo [63], ensuring realistic scene composition. Object scale and motion patterns vary substantially across locations: larger and faster-moving vehicles dominate highways, while smaller and slower agents such as pedestrians and cyclists are more common in urban scenes. This diversity in object type, scale, and dynamics supports a comprehensive evaluation of perception models under varied spatial layouts, motion patterns, and traffic densities.

C. RoScenes Dataset

We further evaluate on the established RoScenes dataset [48], the largest real-world multi-view roadside perception benchmark to date. RoScenes provides an

important complement to M2I by enabling validation under real-world sensor noise, calibration drift, and data imbalance conditions that are difficult to simulate accurately.

RoScenes covers an 800-meter highway segment equipped with 8 synchronized infrastructure-mounted cameras positioned on poles and gantries along the roadside. The dataset contains over 21 million 3D bounding box annotations, capturing diverse traffic flow patterns across normal and heavy traffic. Each scene is annotated with four object categories, including car, van, bus, and truck. The clips are recorded under both daytime and nighttime conditions in clear weather. Although environmental diversity is limited compared to M2I, RoScenes provides realistic visual artifacts such as motion blur, exposure variation, and partial occlusions caused by camera distance and mounting angles.

For validation, the authors curated clips representing the top 10% most occluded and bottom 10% least occluded scenes as hard and easy subsets, respectively. This stratified design allows for controlled evaluation of model performance under varying levels of visual complexity.

By combining M2I’s controlled multi-layout diversity with the RoScenes dataset’s large-scale real-world recordings, we obtain a comprehensive evaluation framework that tests both generalization and robustness across simulated and real roadside domains.

V. EXPERIMENTS

A. Experimental Setup

TABLE II: MIC-BEV Hyperparameters

Hyperparameter	Value	Used In
$H_{\text{bev}}, W_{\text{bev}}$	dataset-specific	BEV Grid
N_{ref}	8	3D Reference Grid / SCA
C (channel dim)	256	All Modules
N_q (object queries)	dataset-specific	DETR Decoder
L (Transformer layers)	6	BEV Transformer
T (temporal context frames)	2	TSA Module
n_{map}	dataset-specific	BEV Segmentation Head
n_{obj}	dataset-specific	BEV Segmentation Head
p_m	0.25	Camera View Masking
λ (segmentation loss weight)	2.0	Loss Function
Dropout (GATv2)	0.1	Camera-BEV GAT
GAT Hidden Dim	128	Camera-BEV GAT
GAT Layers	3	Camera-BEV GAT
GAT Heads	4	Camera-BEV GAT
Seg Decoder Depth	4 Conv Layers	BEV Segmentation Head

TABLE III: Training hyperparameters

Hyperparameter	Value
Learning Rate	2×10^{-4}
Weight Decay	0.01
Batch Size (per GPU)	1
Epochs	10
Warm-up Steps	500
LR Schedule	Cosine Annealing
Minimum LR Ratio	1×10^{-3}
Gradient Clipping	max_norm=1, norm_type=2

Implementation Details. All models are built upon a ResNet-101 backbone with deformable convolutions

TABLE IV: Dataset-specific hyperparameters

Hyperparameter	M2I	RoScenes
Perception Range	$[-51.2, 51.2]^2$	$[-400, 400] \times [-100, 100]$
Post-Center Range	$[-61.2, 61.2]^2$	$[-410, 410] \times [-110, 110]$
Voxel Size (m)	0.2×0.2	0.2×0.2
Grid Size	512×512	4000×1000
BEV Stride	4	4
BEV Size	200×200	1000×250
N_q	200	900
n_{map}	7	—
n_{obj}	4	4
Max Camera Count	4	8

(ResNet101-DCN) as the image encoder. Training is conducted for 10 epochs using the AdamW optimizer with an initial learning rate of 2×10^{-4} and a cosine annealing schedule. Experiments are performed on 8 NVIDIA L40S GPUs with a batch size of 1 per GPU and mixed-precision (FP16) training to reduce memory usage. MIC-BEV hyperparameters are specified in Table II, and model training hyperparameters are summarized in Table III.

Dataset-specific model variations are specified in Table IV. For the M2I dataset, input images are resized to 800×600 pixels, and the BEV grid is defined as 200×200 , covering a $[-51.2, \text{m}, 51.2, \text{m}]$ region along both the X and Y axes. For the RoScenes dataset, input images are kept at 1920×1080 resolution, with a BEV grid of 1000×250 spanning $[-400, \text{m}, 400, \text{m}]$ in X and $[-100, \text{m}, 100, \text{m}]$ in Y. The BEV origin is aligned with either the intersection center or the reference camera position, depending on the scene layout. Since RoScenes lacks semantic maps and LiDAR supervision, BEV segmentation is disabled for this dataset, and only 3D object detection is evaluated.

To assess robustness to sensor degradation in M2I, we apply a controlled view-masking augmentation during testing using the RandomMaskMultiView module. For each sample, one camera view is randomly corrupted by either zeroing the image or applying a Gaussian blur (kernel size 11, $\sigma \in [3.0, 10.0]$). The corruption is applied only when multiple real views are available. To ensure reproducibility, all random operations are deterministically seeded using a hash of the sample identifier, maintaining consistent corruption across runs. This setup enables systematic evaluation of model robustness under degraded or missing views.

Evaluation Metrics. We adopt standard 3D detection metrics from the nuScenes benchmark to evaluate MIC-BEV, including mean Average Precision (mAP) and nuScenes Detection Score (NDS) [62]. To account for object distance and detection fidelity, we report class-wise average precision across a range of distance thresholds. The overall mAP metric is computed as:

$$\text{mAP} = \frac{1}{|\mathcal{C}| \cdot |\mathcal{D}|} \sum_{c \in \mathcal{C}} \sum_{d \in \mathcal{D}} \text{AP}_{c,d}, \quad (11)$$

where \mathcal{C} is the set of object classes, \mathcal{D} is the set of distance thresholds, and $\text{AP}_{c,d}$ is the average precision for class c at distance threshold d .

NDS is a composite score that integrates mAP with five True Positive metrics: mean Average Translation Error (mATE),

TABLE V: Comparison of 3D object detection performance on the **M2I** test set under three evaluation conditions: **Normal**, **Robust** (sensor dropout or degradation), and **Extreme Weather** (heavy rain or fog).

Method	Normal				Robust				Extreme Weather			
	mAP \uparrow	NDS \uparrow	mATE \downarrow	mASE \downarrow	mAP \uparrow	NDS \uparrow	mATE \downarrow	mASE \downarrow	mAP \uparrow	NDS \uparrow	mATE \downarrow	mASE \downarrow
Lift-Splat-Shoot	0.446	0.437	0.742	0.489	0.336	0.371	0.781	0.510	0.367	0.334	0.764	0.631
PETR	0.596	0.595	0.301	0.107	0.415	0.453	0.595	0.156	0.440	0.468	0.689	0.193
BEVFormer	0.637	0.678	0.235	0.072	0.513	0.593	0.288	0.084	0.445	0.452	0.535	0.131
PETRv2	0.651	0.689	0.213	0.093	0.505	0.582	0.295	0.156	0.584	0.588	0.530	0.127
StreamPETR	0.677	0.702	0.211	0.067	0.512	0.579	0.293	0.110	0.591	0.611	0.489	0.102
BEVNeXt	0.681	0.704	0.206	0.069	0.527	0.591	0.291	0.112	0.603	0.617	0.447	0.103
GeoBEV	0.690	0.664	0.203	0.063	0.533	0.576	0.251	0.100	0.623	0.621	0.392	0.110
UVTR	0.698	0.661	0.201	0.062	0.558	0.603	0.220	0.071	0.631	0.639	0.283	0.079
DETR3D	0.701	0.677	0.289	0.056	0.540	0.580	0.338	0.063	0.677	0.661	0.320	0.069
MIC-BEV (Ours)	0.767	0.771	0.179	0.061	0.647	0.678	0.215	0.065	0.709	0.701	0.241	0.077

mean Average Scale Error (mASE), mean Average Orientation Error (mAOE), mean Average Velocity Error (mAVE), and mean Average Attribute Error (mAAE). It provides a balanced evaluation of detection accuracy and localization fidelity:

$$NDS = \frac{1}{10} \left[5 \cdot mAP + \sum_{mTP} (1 - \min(1, mTP)) \right], \quad (12)$$

where $mTP \in \{mATE, mASE, mAOE, mAVE, mAAE\}$.

Baselines. We compare our method against well-established detection models, including Lift-Splat-Shoot (LSS) [16], BEVFormer [24], DETR3D [20], PETR [22], PETRv2 [23], GeoBEV [19], BEVNeXt [28], StreamPETR [25], and UVTR [64]. We do not include RoBEV or RopeBEV in the M2I benchmark due to the lack of available open-source code. These models vary in feature lifting strategies and network architectures but share the same input, providing a fair and competitive benchmark for infrastructure-based 3D perception. To ensure compatibility with variable camera inputs, we apply our padding mechanism to all baselines. The RoScenes benchmark used in our evaluation is adapted from the setup introduced in RopeBEV [51].

B. Results on M2I

Quantitative Evaluation. Table V summarizes the 3D object detection results on the M2I test set under three evaluation settings: *Normal*, *Robust*, and *Extreme Weather*. MIC-BEV achieves state-of-the-art performance across all settings. Under the Normal condition, MIC-BEV attains an mAP of 0.767 and an NDS of 0.771, surpassing the strongest baseline, DETR3D, by more than 9.4% in mAP.

The performance gap becomes more pronounced as input quality degrades. In the Robust setting, where one camera is blurred or missing, MIC-BEV maintains competitive results with 0.647 mAP and 0.678 NDS, corresponding to only a 15.6% performance drop in mAP from the Normal case. In contrast, baseline models such as DETR3D and BEVFormer exhibit degradation of up to 23%. Under Extreme Weather conditions, which include heavy rain and dense fog, MIC-BEV continues to perform the best with 0.709 mAP and 0.701 NDS. Across all settings, MIC-BEV consistently outperforms the strongest competing methods in mAP, achieving state-of-the-art detection accuracy.

These results highlight the efficacy of MIC-BEV’s camera-grid relation-enhanced attention, which enables effective multi-view feature fusion in the BEV space. The M2I benchmark further validates MIC-BEV’s robustness to diverse camera placements and degraded sensor configurations, while demonstrating its ability to detect small and distant objects.

Qualitative Evaluation. Examples of detection and BEV segmentation of MIC-BEV are provided in Fig. 5. As shown in Fig. 6, compared with existing baselines, MIC-BEV reliably identifies objects missed by other methods, corrects misaligned bounding boxes, and suppresses false positives. The BEV segmentation head provides spatial priors that help separate foreground instances from background clutter, improving localization precision. Additionally, camera masking during training simulates partial sensor failures, encouraging the model to utilize complementary viewpoints and thereby enhancing its robustness under occlusion and degraded inputs.

TABLE VI: Per-class object detection results on the M2I testing set (Normal), using mAP as the primary metric.

Method	mAP \uparrow				
	Pedestrian	Truck	Car	Cyclist	Avg.
Lift-Splat-Shoot	0.444	0.397	0.599	0.344	0.446
PETR	0.762	0.573	0.611	0.436	0.596
BEVFormer	0.810	0.623	0.667	0.449	0.637
PETRv2	0.815	0.646	0.679	0.463	0.651
StreamPETR	0.857	0.668	0.687	0.497	0.677
BEVNeXt	0.866	0.670	0.692	0.499	0.681
GeoBEV	0.794	0.719	0.717	0.529	0.690
UVTR	0.768	0.721	0.728	0.577	0.698
DETR3D	0.815	0.689	0.714	0.589	0.701
MIC-BEV	0.860	0.777	0.806	0.626	0.767

Per-class detection performance. Table VI reports the per-class mean average precision (mAP) on the M2I test set under the Normal setting. MIC-BEV achieves the highest accuracy across all object categories. For pedestrians, MIC-BEV achieves 0.860 mAP, surpassing DETR3D and PETRv2 (both 0.815), demonstrating a strong capability in detecting small and dynamic objects. For trucks, MIC-BEV achieves 0.777 mAP, outperforming UVTR (0.721) and reflecting robustness to large and geometrically diverse vehicles. For cars, MIC-BEV attains 0.806 mAP, surpassing UVTR (0.728) and DETR3D (0.714), showing consistent precision in dense scenes. Although cyclist detection remains challenging, MIC-

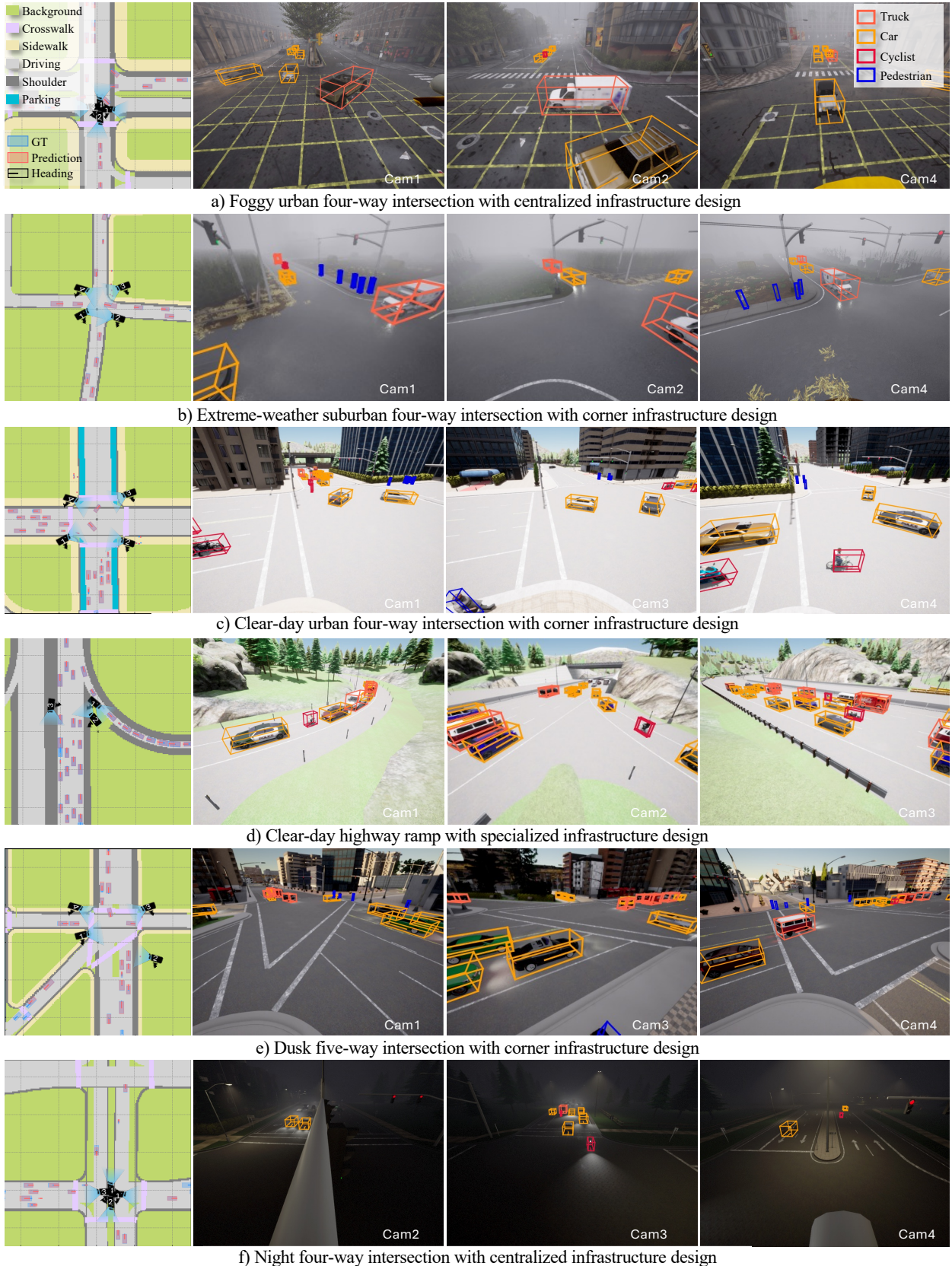


Fig. 5: Qualitative 3D detection results on the M2I dataset. MIC-BEV accurately detects multiple object types across diverse urban scenes with varying traffic densities and weather or lighting conditions.

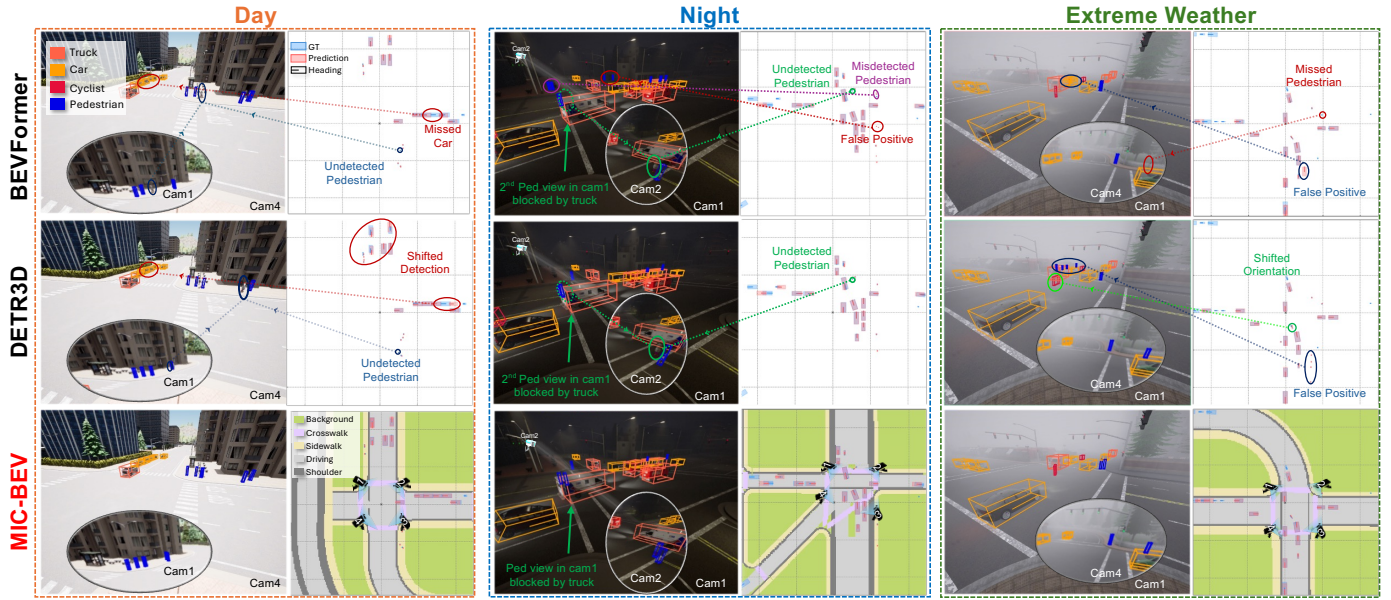


Fig. 6: **Qualitative comparison of MIC-BEV on M2I Dataset with baseline models.** Compared to BEVFormer and DETR3D, MIC-BEV produces more accurate and consistent detections across day, night, and extreme-weather scenes by leveraging relation-aware multi-view fusion. In Intersection 2, a pedestrian partially occluded by a truck is missed by the baselines but successfully detected by MIC-BEV.

TABLE VII: Comparison of 3D object detection performance on the **RoScenes** validation set under **Easy** and **Hard** levels.

Method	Easy					Hard					Average
	mAP \uparrow	NDS \uparrow	mATE \downarrow	mASE \downarrow	mAOE \downarrow	mAP \uparrow	NDS \uparrow	mATE \downarrow	mASE \downarrow	mAOE \downarrow	
SOLOFusion	0.129	0.308	0.878	0.144	0.517	0.066	0.202	0.844	0.144	1.000	0.255
BEVDet4D	0.200	0.428	0.896	0.094	0.041	0.139	0.393	0.922	0.099	0.038	0.411
BEVDet	0.299	0.506	0.742	0.079	0.042	0.184	0.445	0.754	0.087	0.043	0.476
StreamPETR	0.513	0.619	0.690	0.102	0.032	0.284	0.496	0.739	0.107	0.031	0.558
PETRv2	0.587	0.674	0.590	0.090	0.032	0.414	0.580	0.633	0.100	0.029	0.627
BEVFormer	0.609	0.693	0.560	0.078	0.030	0.433	0.597	0.600	0.090	0.029	0.645
DETR3D	0.644	0.722	0.501	0.067	0.031	0.471	0.633	0.508	0.080	0.028	0.678
RoBEV	0.684	0.753	0.442	0.058	0.031	0.524	0.672	0.438	0.077	0.027	0.713
RopeBEV	0.721	0.786	0.435	0.056	0.030	0.545	0.685	0.416	0.078	0.027	0.736
MIC-BEV (Ours)	0.742	0.796	0.220	0.058	0.028	0.561	0.719	0.255	0.077	0.027	0.757

BEV still leads with 0.626 mAP, outperforming DETR3D (0.589) and UVTR (0.577). Overall, MIC-BEV achieves an average mAP of 0.767, substantially higher than all baselines, confirming its ability to generalize across varied layouts and conditions.

C. Results on RoScenes

Table VII presents 3D object detection results on the RoScenes benchmark. MIC-BEV achieves the highest overall performance across both evaluation splits. On the *Easy* set, MIC-BEV attains 0.742 mAP and 0.796 NDS, while on the more challenging *Hard* scenes, it achieves 0.561 mAP and 0.719 NDS, where issues such as severe occlusion, long-range targets, and limited viewpoint overlap are more prevalent.

Compared to RopeBEV, MIC-BEV improves mAP by 3% on both the Easy split and Hard split, while significantly reducing mATE on the Hard scenes by 38.7%. Notably, MIC-BEV shows strong detection capability across the large-scale detection area (800-meter range across eight camera views), reliably detecting distant and densely distributed vehicles in

complex traffic scenarios, which is an essential capability for infrastructure-based perception.

Fig. 7 provides a qualitative comparison of MIC-BEV’s detection results on the RoScenes validation set, visualized across eight synchronized roadside cameras and the corresponding fused BEV view covering an 800-meter detection range. Examples (a)-(b) show daytime scenes on two different highway segments, while (c)-(d) depict twilight and nighttime conditions.

Across all lighting and weather conditions, MIC-BEV produces dense, spatially consistent detections that align well across overlapping camera views. The model successfully detects vehicles at long range, maintains tight bounding boxes even under partial occlusion, and avoids double-counting objects appearing in multiple cameras. In the low-light and nighttime examples, MIC-BEV remains robust to glare, reflection, and headlight bloom, continuing to localize vehicles accurately where baselines often fail or produce fragmented boxes. The fused BEV maps exhibit coherent structure, with clearly separated lanes and minimal false positives in background regions.

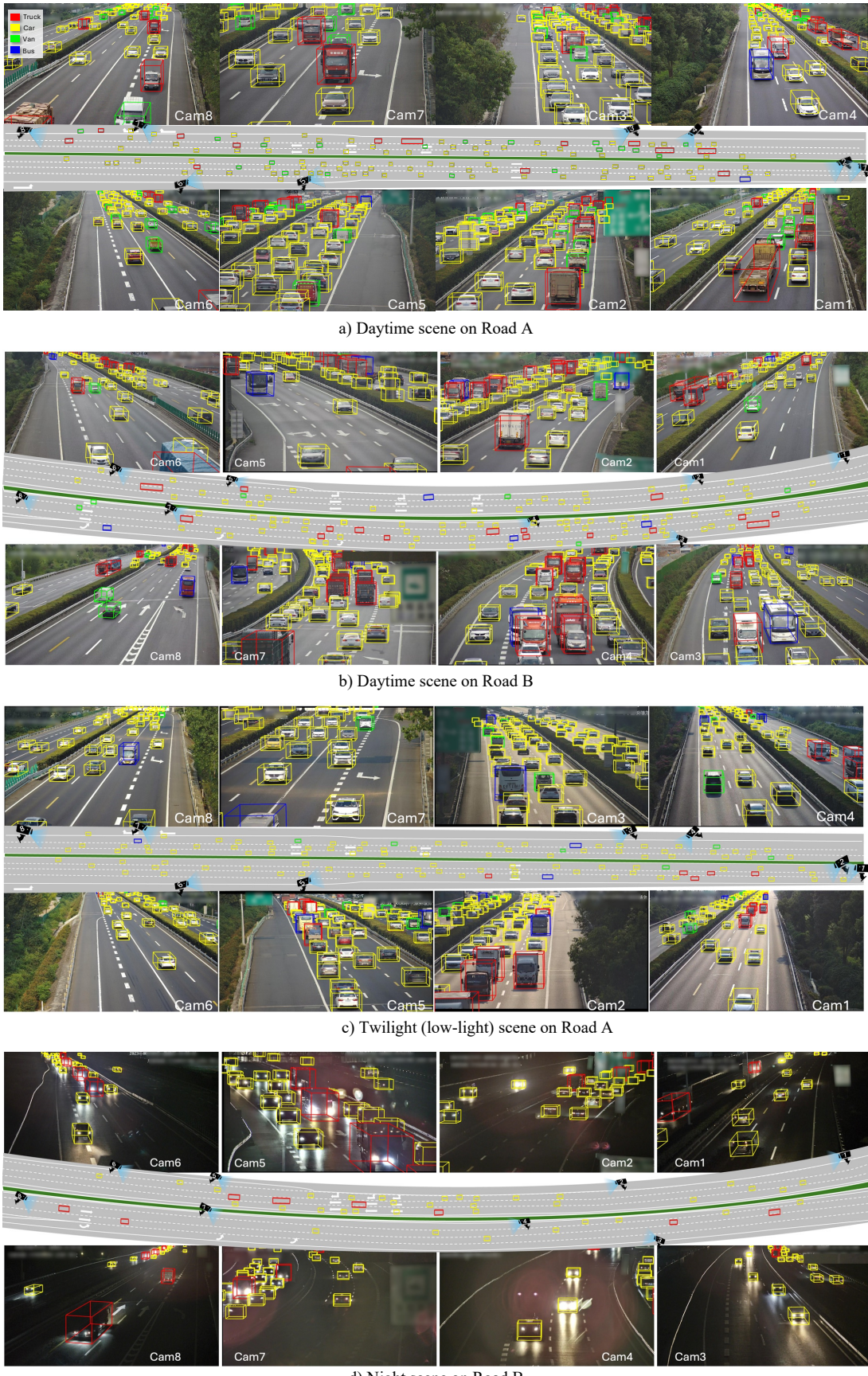


Fig. 7: **Qualitative results of MIC-BEV on the RoScenes validation set.** Each example shows outputs from 8 roadside cameras and the corresponding fused BEV view over an 800-meter range. (a)-(b) depict daytime scenes, while (c)-(d) show twilight and nighttime conditions. MIC-BEV shows strong performance under diverse lighting and camera configurations.

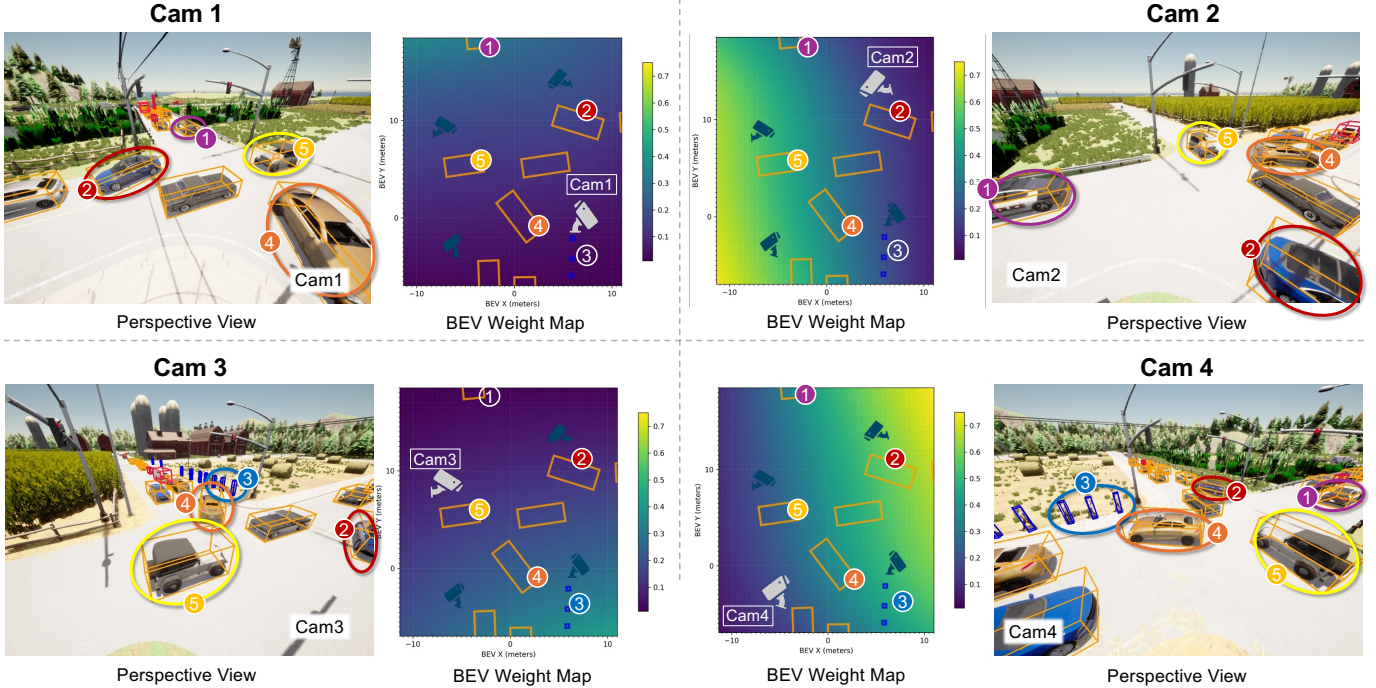


Fig. 8: **Camera-wise importance weights for BEV grid cells at the intersection center.** Each row corresponds to a pair of perspective views and BEV weight maps for Cam1 to Cam4. The BEV maps visualize the spatial contribution of each camera, where warmer colors denote higher weights. Numbered objects (①-⑤) represent key targets selected for detailed analysis. Objects annotated with colored circles (①, ②, ③, ④, ⑤) are visible in the corresponding perspective view, while the same numbered markers without color in other cameras indicate that the objects are occluded or outside the field of view.

These visual results reinforce the quantitative findings, demonstrating that MIC-BEV’s camera-grid relation-enhanced attention effectively aggregates cross-view information and maintains geometric consistency under challenging visibility, large spatial extent, and heterogeneous camera placement.

D. Camera Importance Weight Analysis

Unlike vehicle-mounted cameras, infrastructure cameras often capture scenes from elevated and wide viewpoints, which introduces significant perspective distortions. Objects near the image periphery may appear stretched, foreshortened, or geometrically inconsistent with their true scale. Such distortions directly impact the reliability of spatial cues extracted from each camera view. MIC-BEV’s relation-aware fusion mechanism effectively adapts the contribution of each camera based on viewpoint geometry and object clarity, offering interpretable insights into how spatial reliability is learned.

Fig. 8 illustrates the learned camera-wise importance weights assigned by the GNN in MIC-BEV across four cameras monitoring an intersection. The model consistently assigns higher weights to cameras where objects are clearly visible, centered in the field of view, and minimally distorted. For example, *Object 4* is visible in all four cameras but appears heavily elongated in Cam1 due to an oblique viewing angle. Correspondingly, MIC-BEV assigns a lower weight to Cam1 and emphasizes Cam2 and Cam4, which observe the object from less distorted, more front-facing perspectives. Similarly, *Object 2* is captured in all views but lies near the image

boundary in Cam2 and Cam3, where partial occlusion occurs. The model appropriately prioritizes Cam4, where the object is well-centered and clearly observed.

In the case of *Object 1*, which appears in Cam1, Cam2, and Cam4. However, all views capture it at a distance or near the periphery. Hence, the GNN assigns roughly uniform weights. *Object 3* is visible only in Cam3 and Cam4, both offering direct, minimally occluded views. MIC-BEV assigns balanced and high weights to both cameras. Finally, *Object 5*, seen across all cameras, receives the highest weight from Cam2, which observes the object near the center with the clearest geometric fidelity.

These patterns indicate that MIC-BEV’s GNN does not simply learn a static weight distribution. Rather, it implements an interpretable, geometry-aware process, suppressing distorted or occluded observations while emphasizing geometrically reliable and semantically informative views.

E. Runtime performance

We evaluate inference efficiency on an NVIDIA L40S GPU, comparing MIC-BEV with representative baseline models. As summarized in Table VIII, MIC-BEV achieves an inference speed of 4.65 FPS, which is comparable to BEVFormer (4.76 FPS) and suitable for applications requiring high accuracy. Although lighter models such as LSS (17.52 FPS) and PETR (13.33 FPS) achieve higher frame rates, they incur substantial performance losses, with mAP values below 0.60. This comparison highlights MIC-BEV’s ability to balance detec-

tion accuracy and computational efficiency, achieving superior accuracy while maintaining practical runtime.

TABLE VIII: Comparison of inference speed (frames per second) and mAP on the M2I-Normal testing set.

Model	mAP (M2I-Normal)	FPS
LSS	0.446	17.52
PETR	0.596	13.33
BEVFormer	0.637	4.76
PETRv2	0.651	9.17
StreamPETR	0.677	11.11
BEVNeXt	0.681	10.20
GeoBEV	0.690	6.25
UVTR	0.698	9.09
DETR3D	0.701	11.76
MIC-BEV	0.767	4.65

F. Ablation Studies

1) **Component Ablation:** We perform a component ablation on the M2I test set to evaluate the contribution of each key module in MIC-BEV, including camera masking, the auxiliary BEV segmentation head, and the Relation-Enhanced Spatial Cross-Attention (ReSCA) module. As shown in Table IX, removing any component leads to a consistent performance drop under both the M2I-Normal and M2I-Robust settings.

Enabling random camera masking improves robustness to sensor failures by encouraging the model to rely on complementary camera views. The auxiliary BEV segmentation head further enhances spatial reasoning, providing geometric priors that guide detection. Finally, by studying the effect of the ReSCA module, we replace it with a regular spatial cross-attention layer without graph-based weighting, and observe a clear reduction in both mAP and NDS. This confirms that the GNN weighting mechanism in ReSCA effectively learns view-dependent importance for multi-camera fusion, leading to stronger overall performance.

TABLE IX: Ablation study of MIC-BEV components on the M2I-Normal testing set. *Cam. Masking*: random camera masking; *BEV Seg.*: the auxiliary BEV segmentation head; *ReSCA*: Relation-enhanced spatial cross-attention module

Cam. Masking	BEV Seg.	ReSCA	M2I-Normal		M2I-Robust	
			mAP↑	NDS↑	mAP↑	NDS↑
✗	✗	✗	0.637	0.678	0.513	0.593
✓	✗	✗	0.649	0.689	0.574	0.631
✓	✓	✗	0.691	0.727	0.597	0.647
✓	✓	✓	0.767	0.771	0.647	0.678

2) **Influence of Masking Rate:** We conduct an ablation study to analyze the effect of the view-masking probability p_m during training on the M2I-Normal and Robust testing set. As shown in Table X, applying moderate masking enhances robustness against sensor degradation, while maintaining strong performance under normal conditions. Specifically, when p_m increases from 0.0 to 0.25, the model's mAP for the M2I-Robust set improves by 8%, indicating that exposure to simulated sensor failures effectively encourages the model to rely on complementary visual cues from the remaining views.

However, excessively high masking rates (e.g., $p_m \geq 0.5$) begin to degrade performance on the M2I-Normal set, suggesting that overly frequent view removal limits the model's ability to fully exploit multi-view redundancy. Overall, these results demonstrate that introducing moderate stochastic masking during training provides a favorable balance between standard accuracy and robustness.

TABLE X: Effect of training camera masking probability (p_m) on performance over the M2I normal and robust testing sets.

Masking Rate p_m	mAP↑	
	M2I-Normal	M2I-Robust
0.00	0.764	0.598
0.25	0.767	0.647
0.50	0.757	0.650
0.75	0.742	0.652

3) **Influence of Relation Encoding:** We conduct an ablation study to evaluate the contribution of latent camera features, distance-based relations, and angle-based relations within the GNN-based fusion module. Starting from a baseline that excludes all three components, we observe a mAP of 0.691 and NDS of 0.727. Introducing only geometric relations (distance and angle) without camera features yields a notable improvement (mAP: 0.729, NDS: 0.745), highlighting the importance of spatial structure among infrastructure-mounted cameras. Using only camera features provides comparable gains (mAP: 0.725, NDS: 0.740), indicating that latent image features are beneficial but slightly less effective than geometric relations. Combining camera features with distance relations further boosts performance to 0.761 mAP and 0.765 NDS. The full model, which incorporates all three components, achieves the best results (mAP: 0.767, NDS: 0.771), demonstrating that latent camera features and geometric relations are complementary and essential for multi-view feature fusion.

TABLE XI: Influence of incorporating camera features, distance, and angle relations in the GNN-based multi-view fusion module.

Cam. Feature	Distances	Angles	M2I-Normal	
			mAP↑	NDS↑
✗	✗	✗	0.691	0.727
✗	✓	✓	0.729	0.745
✓	✗	✗	0.725	0.740
✓	✓	✗	0.761	0.765
✓	✓	✓	0.767	0.771

4) **Robustness across Random Seeds:** To evaluate consistency under random perturbations, we assess MIC-BEV's stability across different test-time degradations. The robust test set is constructed by randomly applying image blur or masking one camera view for each sample. We compare MIC-BEV against BEVFormer and DETR3D over three random seeds, reporting the mean and standard deviation of mAP in Table XII. MIC-BEV achieves both the highest average accuracy and the lowest variance, indicating greater stability and reliability under random sensor degradation.

TABLE XII: Detection performance across random seeds for the M2I robust testing set.

Method	M2I-Robust	
	mAP \uparrow	NDS \uparrow
BEVFormer	0.513 \pm 0.009	0.593 \pm 0.008
DETR3D	0.540 \pm 0.007	0.580 \pm 0.008
MIC-BEV	0.647 \pm 0.006	0.678 \pm 0.007

VI. CONCLUSIONS

We propose **MIC-BEV**, a Transformer-based framework for multi-camera infrastructure-based perception, together with **M2I**, a comprehensive synthetic dataset and benchmark encompassing diverse road layouts, camera placements, illumination conditions, and adverse weather. MIC-BEV introduces a **camera-BEV spatial relation-aware attention** mechanism that explicitly models geometric relations between each camera and BEV cell through a graph neural network, enabling adaptive multi-view fusion under heterogeneous configurations. In addition, a dual-level BEV segmentation head jointly learns map-level and object-level priors to enhance spatial reasoning, while camera masking strategies such as random dropout and Gaussian blur improve robustness against sensor degradation, occlusion, and partial failures.

Extensive experiments demonstrate that MIC-BEV consistently achieves state-of-the-art performance across both synthetic (M2I) and real-world (RoScenes) datasets. On M2I, the model shows strong detection accuracy across normal, robust, and extreme weather settings, with a significant improvement in mAP compared to leading baseline methods. On RoScenes, MIC-BEV generalizes effectively to large-scale highway scenes and complex urban intersections, maintaining superior detection stability under limited overlap and challenging lighting. Qualitative analyses further reveal that the relation-enhanced attention dynamically emphasizes informative viewpoints, suppresses redundant or distorted features, and improves the detection of small or distant targets.

Beyond static object detection, future research will focus on extending MIC-BEV toward multi-object tracking and trajectory forecasting to capture dynamic interactions among road users. Another direction is to explore real-time deployment through lightweight backbones and knowledge distillation for edge devices. Finally, we plan to expand the M2I benchmark with additional real-world data to bridge the simulation-to-reality gap and enable comprehensive evaluation across diverse urban contexts.

REFERENCES

- [1] H. Yu, W. Yang, J. Zhong, Z. Yang, S. Fan, P. Luo, and Z. Nie, “End-to-end autonomous driving through v2x cooperation,” *AAAI*, 2025.
- [2] M. Tang, D. Yu, P. Li, C. Song, P. Zhao, W. Xiao, and N. Chen, “A multi-scene roadside lidar benchmark towards digital twins of road intersections,” *ISPRS Annals of the Photogrammetry, Remote Sensing and Spatial Information Sciences*, vol. 10, pp. 341–348, 2024.
- [3] Y. Li, D. Ma, Z. An, Z. Wang, Y. Zhong, S. Chen, and C. Feng, “V2xsim: Multi-agent collaborative perception dataset and benchmark for autonomous driving,” *IEEE Robotics and Automation Letters*, vol. 7, no. 4, pp. 10914–10921, 2022.
- [4] Z. Bai, G. Wu, X. Qi, Y. Liu, K. Oguchi, and M. J. Barth, “Infrastructure-based object detection and tracking for cooperative driving automation: A survey,” in *2022 IEEE Intelligent Vehicles Symposium (IV)*. IEEE, 2022, pp. 1366–1373.
- [5] M. Löttscher, N. Baumann, E. Ghignone, A. Ronco, and M. Magno, “Assessing the robustness of lidar, radar and depth cameras against ill-reflecting surfaces in autonomous vehicles: An experimental study,” in *2023 IEEE 9th World Forum on Internet of Things (WF-IoT)*. IEEE, 2023, pp. 1–6.
- [6] W. Jiang, H. Xiang, X. Cai, R. Xu, J. Ma, Y. Li, G. H. Lee, and S. Liu, “Optimizing the placement of roadside lidars for autonomous driving,” in *Proceedings of the IEEE/CVF International Conference on Computer Vision*, 2023, pp. 18381–18390.
- [7] T.-H. Kim, G.-H. Jo, H.-S. Yun, K.-S. Yun, and T.-H. Park, “Placement method of multiple lidars for roadside infrastructure in urban environments,” *Sensors*, vol. 23, no. 21, p. 8808, 2023.
- [8] L. Kloeker, G. Joeken, and L. Eckstein, “Economic analysis of smart roadside infrastructure sensors for connected and automated mobility,” in *2023 IEEE 26th International Conference on Intelligent Transportation Systems (ITSC)*. IEEE, 2023, pp. 2331–2336.
- [9] W. Wang, Y. Lu, G. Zheng, S. Zhan, X. Ye, Z. Tan, J. Wang, G. Wang, and X. Li, “Bevspread: Spread voxel pooling for bird’s-eye-view representation in vision-based roadside 3d object detection,” in *Proceedings of the IEEE/CVF Conference on Computer Vision and Pattern Recognition*, 2024, pp. 14718–14727.
- [10] L. Yang, X. Zhang, J. Yu, J. Li, T. Zhao, L. Wang, Y. Huang, C. Zhang, H. Wang, and Y. Li, “Monogae: Roadside monocular 3d object detection with ground-aware embeddings,” *IEEE Transactions on Intelligent Transportation Systems*, vol. 25, no. 11, pp. 17587–17601, 2024.
- [11] Z. Li, Z. Chen, A. Li, L. Fang, Q. Jiang, X. Liu, and J. Jiang, “Unsupervised domain adaptation for monocular 3d object detection via self-training,” in *European conference on computer vision*. Springer, 2022, pp. 245–262.
- [12] R. Xu, Z. Tu, H. Xiang, W. Shao, B. Zhou, and J. Ma, “Cobevt: Cooperative bird’s eye view semantic segmentation with sparse transformers,” *arXiv preprint arXiv:2207.02202*, 2022.
- [13] Z. Wu, S. Pan, F. Chen, G. Long, C. Zhang, and P. S. Yu, “A comprehensive survey on graph neural networks,” *IEEE Transactions on Neural Networks and Learning Systems*, vol. 32, no. 1, pp. 4–24, 2021.
- [14] T. Roddick, A. Kendall, and R. Cipolla, “Orthographic feature transform for monocular 3d object detection,” 2018. [Online]. Available: <https://arxiv.org/abs/1811.08188>
- [15] L. Zhang, Y. Liu, X. Wang, Y. He, G. Li, Y. Zhang, C. Liu, Z. Jiang, and Y. Liu, “Caddn: A content-aware downsampling-based detection method for small objects in remote sensing images,” *IEEE Transactions on Geoscience and Remote Sensing*, vol. 63, pp. 1–17, 2025.
- [16] J. Philion and S. Fidler, “Lift, splat, shoot: Encoding images from arbitrary camera rigs by implicitly unprojecting to 3d,” in *European conference on computer vision*. Springer, 2020, pp. 194–210.
- [17] J. Huang, G. Huang, Z. Zhu, Y. Ye, and D. Du, “Bevdet: High-performance multi-camera 3d object detection in bird-eye-view,” *arXiv preprint arXiv:2112.11790*, 2021.
- [18] Y. Li, Z. Ge, G. Yu, J. Yang, Z. Wang, Y. Shi, J. Sun, and Z. Li, “Bevdepth: Acquisition of reliable depth for multi-view 3d object detection,” in *Proceedings of the AAAI conference on artificial intelligence*, vol. 37, 2023, pp. 1477–1485.
- [19] J. Zhang, Y. Zhang, Y. Qi, Z. Fu, Q. Liu, and Y. Wang, “Geobev: Learning geometric bev representation for multi-view 3d object detection,” in *Proceedings of the AAAI Conference on Artificial Intelligence*, vol. 39, no. 9, 2025, pp. 9960–9968.
- [20] Y. Wang, V. C. Guizilini, T. Zhang, Y. Wang, H. Zhao, and J. Solomon, “Det3d: 3d object detection from multi-view images via 3d-to-2d queries,” in *Conference on robot learning*. PMLR, 2022, pp. 180–191.
- [21] N. Carion, F. Massa, G. Synnaeve, N. Usunier, A. Kirillov, and S. Zagoruyko, “End-to-end object detection with transformers,” in *European conference on computer vision*. Springer, 2020, pp. 213–229.
- [22] Y. Liu, T. Wang, X. Zhang, and J. Sun, “Petr: Position embedding transformation for multi-view 3d object detection,” in *European conference on computer vision*. Springer, 2022, pp. 531–548.
- [23] Y. Liu, J. Yan, F. Jia, S. Li, A. Gao, T. Wang, and X. Zhang, “Petr2: A unified framework for 3d perception from multi-camera images,” in *Proceedings of the IEEE/CVF international conference on computer vision*, 2023, pp. 3262–3272.

[24] Z. Li, W. Wang, H. Li, E. Xie, C. Sima, T. Lu, Q. Yu10568349, and J. Dai, “Bevformer: learning bird’s-eye-view representation from lidar-camera via spatiotemporal transformers,” *IEEE Transactions on Pattern Analysis and Machine Intelligence*, 2024.

[25] S. Wang, Y. Liu, T. Wang, Y. Li, and X. Zhang, “Exploring object-centric temporal modeling for efficient multi-view 3d object detection,” in *Proceedings of the IEEE/CVF international conference on computer vision*, 2023, pp. 3621–3631.

[26] J. Huang and G. Huang, “Bevdet4d: Exploit temporal cues in multi-camera 3d object detection,” 2022. [Online]. Available: <https://arxiv.org/abs/2203.17054>

[27] J. Park, C. Xu, S. Yang, K. Keutzer, K. Kitani, M. Tomizuka, and W. Zhan, “Time will tell: New outlooks and a baseline for temporal multi-view 3d object detection,” *arXiv preprint arXiv:2210.02443*, 2022.

[28] Z. Li, S. Lan, J. M. Alvarez, and Z. Wu, “Bevnext: Reviving dense bev frameworks for 3d object detection,” in *Proceedings of the IEEE/CVF conference on computer vision and pattern recognition*, 2024, pp. 20113–20123.

[29] Z. Yang, J. Mao, W. Yang, Y. Ai, Y. Kong, H. Yu, and W. Zhang, “Lidar-based end-to-end temporal perception for vehicle-infrastructure cooperation,” *IEEE Internet of Things Journal*, vol. 12, no. 13, pp. 22862–22874, 2025.

[30] W. Zimmer, J. Wu, X. Zhou, and A. C. Knoll, “Real-time and robust 3d object detection with roadside lidars,” in *Proceedings of the 12th International Scientific Conference on Mobility and Transport: Mobility Innovations for Growing Megacities*. Springer, 2023, pp. 199–219.

[31] H. Yu, Y. Tang, E. Xie, J. Mao, J. Yuan, P. Luo, and Z. Nie, “Vehicle-infrastructure cooperative 3d object detection via feature flow prediction,” 2023. [Online]. Available: <https://arxiv.org/abs/2303.10552>

[32] W. Zimmer, J. Birkner, M. Brucker, H. T. Nguyen, S. Petrovski, B. Wang, and A. C. Knoll, “Infradet3d: Multi-modal 3d object detection based on roadside infrastructure camera and lidar sensors,” in *2023 IEEE Intelligent Vehicles Symposium (IV)*. IEEE, 2023, pp. 1–8.

[33] X. Bai, Z. Hu, X. Zhu, Q. Huang, Y. Chen, H. Fu, and C.-L. Tai, “Transfusion: Robust lidar-camera fusion for 3d object detection with transformers,” in *Proceedings of the IEEE/CVF conference on computer vision and pattern recognition*, 2022, pp. 1090–1099.

[34] Z. Liu, H. Tang, A. Amini, X. Yang, H. Mao, D. Rus, and S. Han, “Bevfusion: Multi-task multi-sensor fusion with unified bird’s-eye view representation,” *arXiv preprint arXiv:2205.13542*, 2022.

[35] Z. Meng, Y. Zhang, Z. Zheng, Z. Zhao, and J. Ma, “Agentalign: Misalignment-adapted multi-agent perception for resilient inter-agent sensor correlations,” *arXiv preprint arXiv:2412.06142*, 2024.

[36] H. Hu, Z. Liu, S. Chitlangia, A. Agnihotri, and D. Zhao, “Investigating the impact of multi-lidar placement on object detection for autonomous driving,” in *Proceedings of the IEEE/CVF conference on computer vision and pattern recognition*, 2022, pp. 2550–2559.

[37] Z. Zheng, Y. Zhang, Z. Meng, J. Liu, X. Xia, and J. Ma, “Insp: Rapid evaluation of heterogeneous multi-modal infrastructure sensor placement,” 2025.

[38] X. Ye, M. Shu, H. Li, Y. Shi, Y. Li, G. Wang, X. Tan, and E. Ding, “Rope3d: The roadside perception dataset for autonomous driving and monocular 3d object detection task,” in *Proceedings of the IEEE/CVF Conference on Computer Vision and Pattern Recognition*, 2022, pp. 21341–21350.

[39] H. Yu, Y. Luo, M. Shu, Y. Huo, Z. Yang, Y. Shi, Z. Guo, H. Li, X. Hu, J. Yuan *et al.*, “Dair-v2x: A large-scale dataset for vehicle-infrastructure cooperative 3d object detection,” in *Proceedings of the IEEE/CVF conference on computer vision and pattern recognition*, 2022, pp. 21361–21370.

[40] L. Yang, K. Yu, T. Tang, J. Li, K. Yuan, L. Wang, X. Zhang, and P. Chen, “Bevheight: A robust framework for vision-based roadside 3d object detection,” in *Proceedings of the IEEE/CVF Conference on Computer Vision and Pattern Recognition*, 2023, pp. 21611–21620.

[41] L. Yang, T. Tang, J. Li, K. Yuan, K. Wu, P. Chen, L. Wang, Y. Huang, L. Li, X. Zhang *et al.*, “Bevheight++: Toward robust visual centric 3d object detection,” *IEEE Transactions on Pattern Analysis and Machine Intelligence*, 2025.

[42] H. Shi, C. Pang, J. Zhang, K. Yang, Y. Wu, H. Ni, Y. Lin, R. Stiefelhagen, and K. Wang, “Cobev: Elevating roadside 3d object detection with depth and height complementarity,” *IEEE Transactions on Image Processing*, 2024.

[43] J. Jinrang, Z. Li, and Y. Shi, “Monouni: A unified vehicle and infrastructure-side monocular 3d object detection network with sufficient depth clues,” *Advances in Neural Information Processing Systems*, vol. 36, pp. 11703–11715, 2023.

[44] W. Chen, Y. Su, J. Zuo, C. Yang, C. Yuan, C. Qian, C.-M. Chan, Y. Qin, Y. Lu, R. Xie *et al.*, “Agentverse: Facilitating multi-agent collaboration and exploring emergent behaviors in agents,” *arXiv preprint arXiv:2308.10848*, vol. 2, no. 4, p. 6, 2023.

[45] G. Liu, Y. Hu, C. Xu, W. Mao, J. Ge, Z. Huang, Y. Lu, Y. Xu, J. Xia, Y. Wang *et al.*, “Towards collaborative autonomous driving: Simulation platform and end-to-end system,” *IEEE Transactions on Pattern Analysis and Machine Intelligence*, 2025.

[46] H. Xiang, Z. Zheng, X. Xia, R. Xu, L. Gao, Z. Zhou, X. Han, X. Ji, M. Li, Z. Meng *et al.*, “V2x-real: a large-scale dataset for vehicle-to-everything cooperative perception,” in *European Conference on Computer Vision*. Springer, 2024, pp. 455–470.

[47] R. Hao, S. Fan, Y. Dai, Z. Zhang, C. Li, Y. Wang, H. Yu, W. Yang, J. Yuan, and Z. Nie, “Rcooper: A real-world large-scale dataset for roadside cooperative perception,” in *Proceedings of the IEEE/CVF conference on computer vision and pattern recognition*, 2024, pp. 22347–22357.

[48] X. Zhu, H. Sheng, S. Cai, B. Deng, S. Yang, Q. Liang, K. Chen, L. Gao, J. Song, and J. Ye, “Roscenes: A large-scale multi-view 3d dataset for roadside perception,” in *European Conference on Computer Vision*. Springer, 2024, pp. 331–347.

[49] S. Fan, Z. Wang, X. Huo, Y. Wang, and J. Liu, “Calibration-free bev representation for infrastructure perception,” in *2023 IEEE/RSJ International Conference on Intelligent Robots and Systems (IROS)*. IEEE, 2023, pp. 9008–9013.

[50] A. Vaghela, D. Lu, A. A. Verma, B. Chakravarthi, H. Wei, and Y. Yang, “Mc-beviro: Multi-camera bird eye view road occupancy detection for traffic monitoring,” *arXiv preprint arXiv:2502.11287*, 2025.

[51] J. Jia, G. Yi, and Y. Shi, “Ropebev: A multi-camera roadside perception network in bird’s-eye-view,” *arXiv preprint arXiv:2409.11706*, 2024.

[52] K. He, X. Zhang, S. Ren, and J. Sun, “Deep residual learning for image recognition,” in *Proceedings of the IEEE conference on computer vision and pattern recognition*, 2016, pp. 770–778.

[53] T.-Y. Lin, P. Dollár, R. Girshick, K. He, B. Hariharan, and S. Belongie, “Feature pyramid networks for object detection,” in *Proceedings of the IEEE conference on computer vision and pattern recognition*, 2017, pp. 2117–2125.

[54] X. Zhu, W. Su, L. Lu, B. Li, X. Wang, and J. Dai, “Deformable DETR: Deformable transformers for end-to-end object detection,” *arXiv preprint arXiv:2010.04159*, 2020.

[55] P. Veličković, G. Cucurull, A. Casanova, A. Romero, P. Lio, and Y. Bengio, “Graph attention networks,” *arXiv preprint arXiv:1710.10903*, 2017.

[56] S. Brody, U. Alon, and E. Yahav, “How attentive are graph attention networks?” *arXiv preprint arXiv:2105.14491*, 2021.

[57] R. Xu, H. Xiang, Z. Tu, X. Xia, M.-H. Yang, and J. Ma, “V2x-vit: Vehicle-to-everything cooperative perception with vision transformer,” in *European conference on computer vision*. Springer, 2022, pp. 107–124.

[58] Z. Zhou, H. Xiang, Z. Zheng, S. Z. Zhao, M. Lei, Y. Zhang, T. Cai, X. Liu, J. Liu, M. Bajji *et al.*, “V2xpn: Vehicle-to-everything spatio-temporal fusion for multi-agent perception and prediction,” *arXiv preprint arXiv:2412.01812*, 2024.

[59] W. Zimmer, G. A. Wardana, S. Sritharan, X. Zhou, R. Song, and A. C. Knoll, “Tumtrat v2x cooperative perception dataset,” in *Proceedings of the IEEE/CVF conference on computer vision and pattern recognition*, 2024, pp. 22668–22677.

[60] H. Xiang, Z. Zheng, X. Xia, S. Z. Zhao, L. Gao, Z. Zhou, T. Cai, Y. Zhang, and J. Ma, “V2x-real: An open online framework and dataset for cooperative perception in reality,” *ECCV*, 2024.

[61] A. Dosovitskiy, G. Ros, F. Codevilla, A. Lopez, and V. Koltun, “Carla: An open urban driving simulator,” in *Conference on robot learning*. PMLR, 2017, pp. 1–16.

[62] H. Caesar, V. Bankiti, A. H. Lang, S. Vora, V. E. Liou, Q. Xu, A. Krishnan, Y. Pan, G. Baldan, and O. Beijbom, “nuscenes: A multimodal dataset for autonomous driving,” in *Proceedings of the IEEE/CVF conference on computer vision and pattern recognition*, 2020, pp. 11621–11631.

[63] P. Sun, H. Kretzschmar, X. Dotiwalla, A. Chouard, V. Patnaik, P. Tsui, J. Guo, Y. Zhou, Y. Chai, B. Caine *et al.*, “Scalability in perception for autonomous driving: Waymo open dataset,” in *Proceedings of the IEEE/CVF conference on computer vision and pattern recognition*, 2020, pp. 2446–2454.

[64] Y. Li, Y. Chen, X. Qi, Z. Li, J. Sun, and J. Jia, “Unifying voxel-based representation with transformer for 3d object detection,” *Advances in Neural Information Processing Systems*, vol. 35, pp. 18442–18455, 2022.